

Article

Correlation between Defect Density and Corrosion Parameter of Electrochemically Oxidized Aluminum

Hao-Ren Lou ¹, Dah-Shyang Tsai ^{1,*}  and Chen-Chia Chou ²

¹ Department of Chemical Engineering, National Taiwan University of Science and Technology, 43, Keelung Road, Section 4, Taipei 10607, Taiwan; m10606011@mail.ntust.edu.tw

² Department of Mechanical Engineering, National Taiwan University of Science and Technology, 43, Keelung Road, Section 4, Taipei 10607, Taiwan; ccchou@mail.ntust.edu.tw

* Correspondence: dstsai@mail.ntust.edu.tw; Tel.: +886-2-2737-6618

Received: 5 December 2019; Accepted: 24 December 2019; Published: 27 December 2019



Abstract: It has been recognized that a connection may exist between defects of oxide coating and its corrosion protection. Such a link has not been substantiated. We prepare two coatings of anodized aluminum oxide (AAO) and plasma electrolytic oxidation (PEO), and analyze them with Mott-Schottky plots and potentiodynamic polarization scans. The as-grown and annealed AAO coatings exhibit both p-type and n-type semiconductor behaviors. Polarization resistance of the AAO coating increases from $(1.8 \pm 1.7) \times 10^8$ to $(4.3 \pm 0.5) \times 10^8 \Omega \cdot \text{cm}^2$, while corrosion current decreases from $(6.1 \pm 3.6) \times 10^{-7}$ to $(2.3 \pm 0.9) \times 10^{-7} \text{ A} \cdot \text{cm}^{-2}$, as annealing temperature increases from room temperature to 400 °C. The parameter analysis on AAO indicates a positive correlation between corrosion current and donor density, a negative correlation between polarization resistance and donor density. The attempt on correlating corrosion potential gives rise to considerable deviation from a linear fit. The results suggest protection of AAO hinges on its donor density, not acceptor. On the PEO coatings, only the n-type behavior is observed. Intriguingly, the donor density of PEO coating is influenced by the annealing temperature of its pre-anodized layer. The most resistant PEO coating, with pre-anodized and 400 °C annealed AAO, exhibits polarization resistance $(2.1 \pm 0.4) \times 10^9 \Omega \cdot \text{cm}^2$ and corrosion current $(1.7 \pm 0.4) \times 10^{-8} \text{ A} \cdot \text{cm}^{-2}$.

Keywords: anodized aluminum; corrosion resistance; Mott-Schottky analysis; defect; annealing; plasma electrolytic oxidation

1. Introduction

Electrochemical oxidation offers several value-added attributes to the aluminum surface such as color, hardness, corrosion, and scratch resistances, which enhance its aesthetic and functional purposes. In industrial practice, oxidation of the surface is performed through anodizing or plasma electrolytic oxidation (PEO). Anodizing is commonly carried out in acidic solutions, with an imposed voltage sufficiently low such that electric discharges did not occur. When the imposed voltage is raised to a point that electric discharges emerge and travel on the metal surface, the processing enters the phase of PEO [1–5]. However, the division between anodizing and PEO may not be as clear-cut as described. For example, the treatment of PEO is usually performed in alkaline electrolytic solutions using the constant current mode. The metal surface has to go through a voltage escalating period to reach the state of traveling microdischarges. Thus, PEO is often preceded by a brief period of anodizing.

Anodizing may produce two morphologies of anodic aluminum oxide (AAO): self-ordered porous films and non-porous compact barrier films. In the last two decades, the anodic aluminum oxide composed of regular nanometer pores has attracted tremendous attention, since researchers are in a fervent pursuit of well-defined porous templates that allow them to mold their nanomaterials.

The studies on porous-type film have yielded detailed knowledge on how electric current and solution composition can be varied to control the pore size, the interpore spacing, and even the pore diameter in vertical direction [6,7]. On the other hand, a barrier-type film of planar geometry is also desirable. The compact barrier layer with high dielectric strength finds its applications in the electronic devices of metal-insulator-metal capacitor and the microfluidic devices of electrowetting on dielectrics [8,9].

The morphological dissimilarity between porous- and barrier-type films arises from a high-to-low level of incorporating electrolyte anions (highest for regular-pore films, least for non-porous barrier films). In the acidic electrolyte, the incorporating anions could be SO_4^{2-} , $\text{C}_2\text{O}_4^{2-}$, or PO_4^{3-} . In the neutral or alkaline electrolyte, the anion is the hydroxyl group [6]. Despite the notable morphology differences [10–12], a few aspects are in common. Those oxygen-carrying anions migrate inward, driven by an imposed electric field. Outward migrating Al^{3+} cations diffuse in the opposite direction and both contribute to oxide growth. Both the porous- and the barrier-type films are featured with a barrier layer, which is the oxide adjacent to metallic substrate.

Ion migration in the oxide coating is made possible by point defects. The barrier layer may be viewed as semiconductor because of these frozen point defects [13–16]. When soaked in an electrolytic solution, the barrier layer has two interfaces: the oxide/electrolyte and oxide/metal interfaces. In the AAO literature, researchers concur on the physical picture that one interface is p-type and the other n-type, but cannot agree upon which side is p-type or n-type. The review article of Diggle [17], along with the works of Takahashi [18] and Mibus [19], assumed that the region near oxide/electrolyte interface was anion excess in stoichiometry, therefore, the p-type region. The inner region of oxide/metal interface was excess in metallic cation and n-type behavior. An opposite view was given in the works of Vrublevsky [20–23] and also Benfedda [24], who considered that negative charges such as electrons were trapped at the oxide/electrolyte interface and acted as donors for the n-type behavior. Positive charges, such as holes, were trapped at the oxide/metal interface, acting as acceptors responsible for the p-type behavior.

Researchers have recognized the connection between defects and corrosion and formulated three mechanisms to account for corrosion current via electron and proton conduction [25–27]. Nonetheless, a straightforward correlation of experimental data, to the best of our knowledge, is not reported. Corrosion of the anodized Al alloy 6061 may serve as an excellent example, since 6061 is widely used as structural materials in the aviation and marine industries, and extensively attacked in a chloride containing environment. In this work, we prepare a dense and conformal barrier layer on the 6061 surface. The oxide coating displays the n-type and the p-type behaviors both. We vary the dopant densities with thermal annealing, and show that the corrosion resistance of oxide coating can be correlated to the defect density of donor, not acceptor. Further discussion indicates the external interface of coating is n-type, responsible to the corrosion protection. On the other hand, the inner interface is p-type and is largely related to the growth behavior.

2. Materials and Methods

Two types of coatings on 6061 aluminum alloy were prepared: the AAO coating and the PEO coating with pre-anodized oxide. Anodization of the pre-cleaned surface was performed with a pulsed current of square bipolar waveform in the aqueous solution of $5.5 \text{ g}\cdot\text{dm}^{-3}$ ammonium pentaborate octahydrate ($\text{NH}_4\text{B}_5\text{O}_8\cdot 8\text{H}_2\text{O}$). The pH value of electrolytic solution was 8.6 and its conductivity $1.45 \text{ mS}\cdot\text{cm}^{-1}$ at room temperature. The electrical parameters of potentiostatic anodization were set as follows: 200 V in positive polarization and 40 V in negative polarization, 50 Hz in frequency, and 40% in duty ratio. This set of electrical parameters were abbreviated as 200 V (+)/40 V (–), which did not give rise to electrical discharges throughout anodization. The frequency was defined as $(T_{\text{on}}^+ + T_{\text{off}}^+ + T_{\text{on}}^- + T_{\text{off}}^-)^{-1}$, in which T_{on}^+ and T_{on}^- were the duration periods of positive and negative pulses, respectively. T_{off}^+ and T_{off}^- were the resting periods between the positive and negative pulses. The duty ratio was defined as $T_{\text{on}}^+ / (T_{\text{on}}^+ + T_{\text{off}}^+ + T_{\text{on}}^- + T_{\text{off}}^-)$. The anodization period of 200 V (+)/40 V (–) was 20 min. Most of anodized samples were annealed, then subject to the galvanostatic

PEO treatment. A few anodized samples were etched in sulfuric acid. The parameters of subsequent PEO were set $45.3 \text{ mA}\cdot\text{cm}^{-2}$ (0.7 A) for positive polarization and $51.8 \text{ mA}\cdot\text{cm}^{-2}$ (0.8 A) for negative polarization, with frequency 50 Hz and duty 40%. This set of PEO parameters was abbreviated as 0.7 A (+)/0.8 A (–). The entire PEO treatment lasted two min and the cell voltage was recorded. In electrochemical oxidations, the sample was mounted at the central position of the electrolytic solution, and the electrical current was sent by a direct current (DC) power supply (DCG-100A, ENI Emerson Electric Co., Saint Louis, MO, USA) with a pulse waveform generator (SPIK-2000A-10H, MELEC, GmbH, Shanghai, China). More details on the setup of anodization and PEO, Figure S1, along with the working procedure, Figure S2, can be found in Supplementary Materials and our previous publication [28].

Annealing of the anodized sample was executed in flowing nitrogen at 100, 150, 250, 300, and 400 °C for one hour using a tubular reactor. Etching of a few anodized samples was performed in 2.0 M sulfuric acid for 15, 30, 45, and 60 min. These samples were subject to Mott-Schottky analysis before etching. The analysis procedure was repeated after etching and washing. For Mott-Schottky analysis, the capacitance in aqueous solutions was recorded every 0.05 V between +2.0 and –2.0 V (vs. Ag/AgCl). The value of space charge capacitance was calculated as the inverse of the imaginary component of impedance at 1 kHz, which was recorded with an electrochemical workstation (Autolab PGSTAT302N, Herisau, Switzerland). Given that double-layer capacitance exceeds space charge capacitance sufficiently and the two are in series, the measured capacitance is dominated by the value of space charge capacitance. The three-electrode setup of impedance measurement involved a solution of $5.5 \text{ g}\cdot\text{dm}^{-3}$ $\text{NH}_4\text{B}_5\text{O}_8$ housed in a 500 mL beaker, with the reference electrode of Ag/AgCl (3.0 M KCl) and the counter electrode of stainless mesh. The working electrode of anodized sample was placed at the beaker center, surrounded by the stainless mesh electrode, and was 7.6 cm in diameter. The Ag/AgCl reference was located adjacent to the working electrode.

The surface morphology was examined with a field-emission scanning electron microscope (SEM, JSM-7900F, JEOL, Tokyo, Japan). The surfaces were metallized with platinum prior to SEM observations. The coating thickness was taken as the average value of six different locations of the mounted specimen. Phase analysis was performed with a wide-angle X-ray diffractometer (D2 phaser, Bruker, Billerica, MA, USA), equipped with a $\text{CuK}\alpha_1$ radiation source and nickel filter. Diffraction results are plotted in Supplementary Materials. Corrosion resistance was evaluated using the technique of potentiodynamic polarization scan. The measurement was done in a solution of 3.5% sodium chloride at room temperature with a three-electrode setup. The setup involved a working electrode with an exposed area 1.0 cm^2 , a reference electrode Ag/AgCl (1.0 M KCl), and a counter electrode of platinum coated titanium mesh $20 \text{ mm} \times 20 \text{ mm}$. Potentiodynamic polarization data were taken using a 1287A electrochemical interface (Solartron Analytical, Leicester, UK). Current data were recorded between –2.0 and 0.0 V at scan rate $5 \text{ mV}\cdot\text{s}^{-1}$. The corrosion current (J_{corr}) and the corrosion potential (E_{corr}) were read from the intersection point of anodic and cathodic extrapolated Tafel lines. With the anodic and cathodic Tafel slopes, b_a and b_c , the polarization resistance (R_p) was calculated with the Stern-Geary equation as shown in Equation (1).

$$R_p = \frac{b_a \times b_c}{2.303 \times J_{\text{corr}} \times (b_a + b_c)} \quad (1)$$

3. Results and Discussion

3.1. Defect Density and Corrosion Protection of AAO

Figure 1a,b shows the cross-sectional and top-view images of as-grown barrier layer. As expected, the AAO layer is nonporous and compliant, with minor surface undulations due to scratches left after polishing. There is no discharge damage found in the oxide since no spark has occurred under 200 V (+)/40 V (–) in the pH 8.6 solution. Thickness of the barrier layer is measured $286 \pm 30 \text{ nm}$. The time profiles of positive and negative current, Figure 1c, are consistent with the literature description on

self-limiting growth [6]. As time progresses, the positive current density decreases exponentially from an initial value $16.2 \text{ mA}\cdot\text{cm}^{-2}$ to a steady value $0.65 \text{ mA}\cdot\text{cm}^{-2}$. Similarly, the negative current descends from an initial value $4.53 \text{ mA}\cdot\text{cm}^{-2}$ to a steady one, $0.65 \text{ mA}\cdot\text{cm}^{-2}$. The self-limiting growth occurs when the metal piece is made an anode in the electrolytic solution that furnishes oxygen-containing species, and then a film develops uniformly to oppose the ongoing growth since the dielectric film obstructs diffusion of ions, along with their associated charge-transfer reactions. Consequently, holding the voltage constant, the current diminishes with increasing oxide thickness. If the defect concentration of newly-added oxide is the same with that of grown oxide, the barrier layer resistance increases linearly with the layer thickness and the electric current drops exponentially. Hence, the final thickness of barrier layer is largely determined by the imposed voltage, irrelevant to anodization time. The ratio of layer thickness over applied voltage has been reported $1.1\text{--}1.4 \text{ nm}\cdot\text{V}^{-1}$ in literature [9,29], depending on the electrolytic solution. Oxide growth of our $200 \text{ V (+)}/40 \text{ V (-)}$ anodization obeys this rule of thumb, showing a ratio of AAO thickness divided by imposing voltage, $\sim 1.4 \text{ nm}\cdot\text{V}^{-1}$.

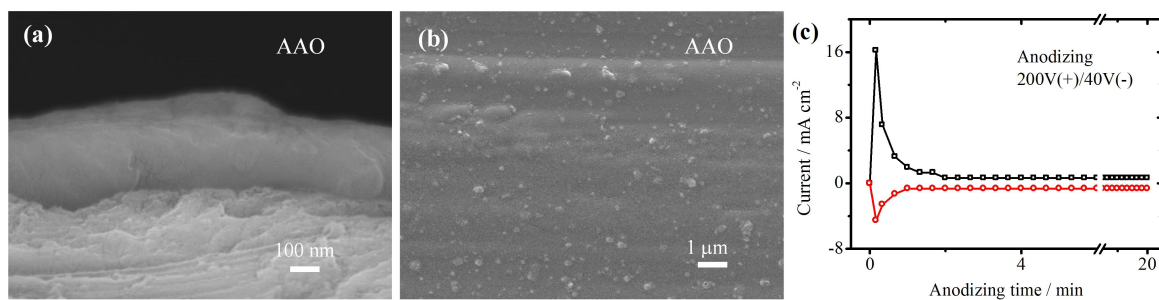


Figure 1. Morphological qualities of the AAO layer and the current density profile in anodizing. The images of (a) cross-sectional view and (b) top view for the barrier layer grown in the solution of $5.5 \text{ g}\cdot\text{dm}^{-3} \text{ NH}_4\text{B}_5\text{O}_8\cdot 8\text{H}_2\text{O}$. The associated (c) anodizing current is performed with the potentiostatic condition $200 \text{ V (+)}/40 \text{ V (-)}$.

Crystal defects provide the essential diffusion channels during growth. After anodization, these remaining defects are vital to the properties of barrier layer. Thermal annealing is known to diminish the defect density of oxide effectively. Figure 2 shows a series of Mott-Schottky plots for the six samples with low-to-high annealing temperature. For each plot of the inverse square of space charge capacitance C_{SC}^{-2} versus electrode potential E , the acceptor density N_a or the donor density N_d can be extracted from the slope of linear segment, as shown in Equations (2) and (3).

$$C_{\text{SC}}^{-2} = \frac{-2}{\epsilon\epsilon_0eN_a}(E - E_{\text{fb}} - \frac{kT}{e}), \text{ p-type} \quad (2)$$

$$C_{\text{SC}}^{-2} = \frac{2}{\epsilon\epsilon_0eN_d}(E - E_{\text{fb}} - \frac{kT}{e}), \text{ n-type} \quad (3)$$

in which ϵ and ϵ_0 denote the relative dielectric constant and the vacuum permittivity, κ is the Boltzmann constant, T is the absolute temperature, e is the electrical charge and E_{fb} is the flat-band potential. For each annealing temperature in Figure 2, one cave-in of the C_{SC}^{-2} - E plot can be found around the electrode potential -0.6 V . Another cave-in may be detected at the more negative potential, related to hydrogen evolution reaction. The cave-in of V-shape indicates the p-type and n-type defects both exist in the barrier layer, since two correlation lines of negative and positive slopes can be drawn. Thus the anodized barrier layer is a p-n heterojunction that may be separated by a neutral region, consistent with the literature. The two slopes generally increase, with increasing annealing temperature. In other words, the acceptor and donor densities decrease. Of the two correlation lines, the intersection potential is assumed to be the flat-band potential value. The E_{fb} value shifts with annealing temperature in the positive direction from -1.4 (as-grown), -0.67 (100°C), -0.66 (150°C), -0.53 (250°C), -0.52 (300°C), -0.50 V (400°C), suggesting the defects of barrier layer shift in a systematic manner.

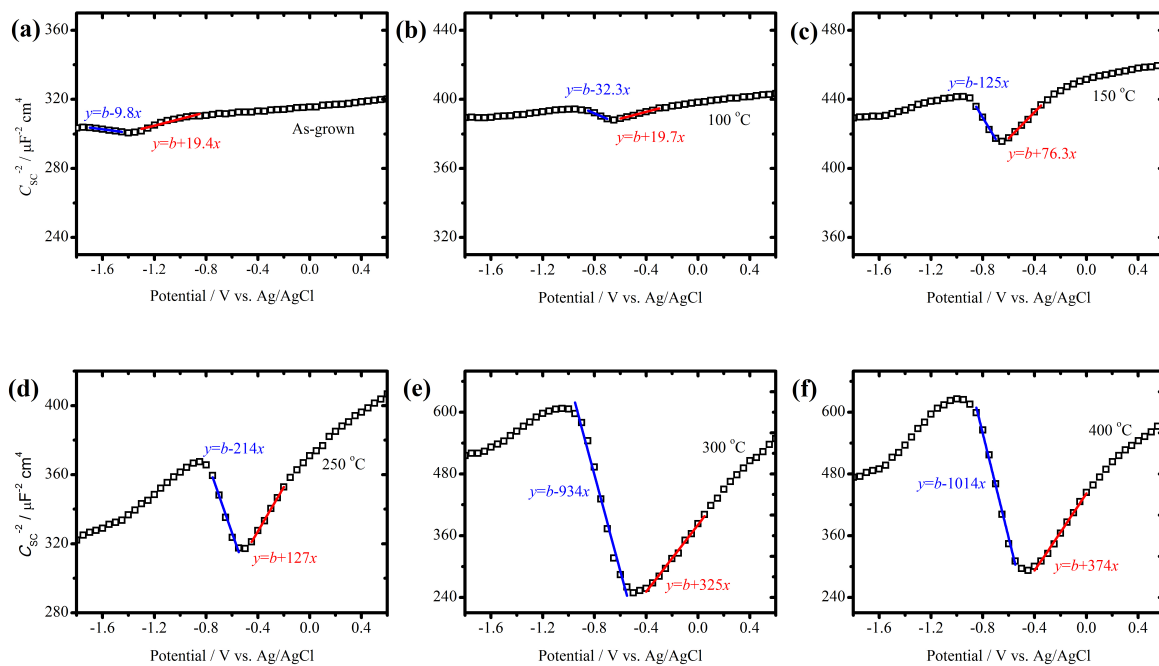


Figure 2. Mott-Schottky plots of annealed AAO layers. The inverse square of space charge capacitance is plotted versus electrode potential between -1.8 and 0.6 V for the (a) as-grown barrier layer, the barrier layers after annealing at (b) 100 , (c) 150 , (d) 250 , (e) 300 , (f) 400 °C for 1 h. The positive and negative slopes of linear segment are marked.

Acceptor and donor densities decrease with increasing annealing temperature, as shown in Figure 3. The acceptor density N_a is higher than the donor density N_d in the as-grown barrier layer. Meanwhile, the acceptor density exhibits a higher temperature dependence than the donor density, that is, annealing decreases the acceptor density faster than the donor density. Annealing at 100 °C is sufficient to reduce the acceptor density from 1.7×10^{18} (as-grown) to 5.2×10^{17} cm^{-3} . On the other hand, the donor density decreases slightly from 8.6×10^{17} to 8.4×10^{17} cm^{-3} . The significant drop in donor density occurs at the higher annealing temperature of 150 °C. Further decline in the defect density is less drastic with increasing temperature. The N_a value of 300 °C sample 1.8×10^{16} cm^{-3} is near that of 400 °C, 1.6×10^{16} cm^{-3} . The N_d values of 300 and 400 °C are similar in magnitude as well, with 5.1×10^{16} (300 °C) and 4.4×10^{16} cm^{-3} (400 °C).

Figure 4a presents the typical potentiodynamic polarization curves of annealed barrier layers, in contrast to those of the as-grown barrier layer and the 6061 surface with natural oxide. Comparison of these polarization curves indicates that thermal annealing improves corrosion protection of the barrier layer against 3.5% NaCl solution. Raising the annealing temperature diminishes the corrosion current J_{corr} , raises the polarization resistance R_p , and shifts the corrosion potential E_{corr} in the positive direction. The improvement on anticorrosion appears to be progressive among annealed samples. The most visible enhancement is noted between the as-grown barrier layer and the natural oxide on 6061 surface, yet the overall improvement through annealing is also impressive.

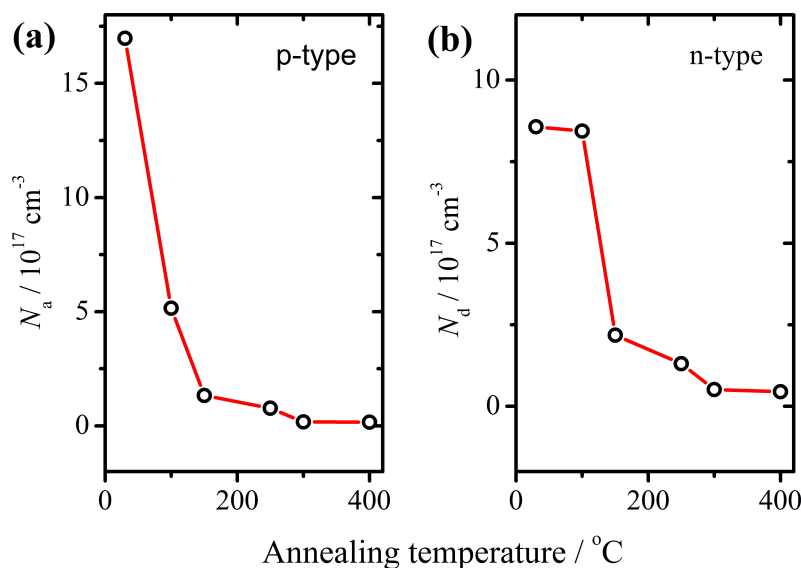


Figure 3. Defect densities of the AAO layer plotted against the annealing temperature. The defect densities of (a) acceptor and (b) donor decrease with increasing annealing temperature. The annealing temperature of as-grown barrier layer is assigned to be 30 °C.

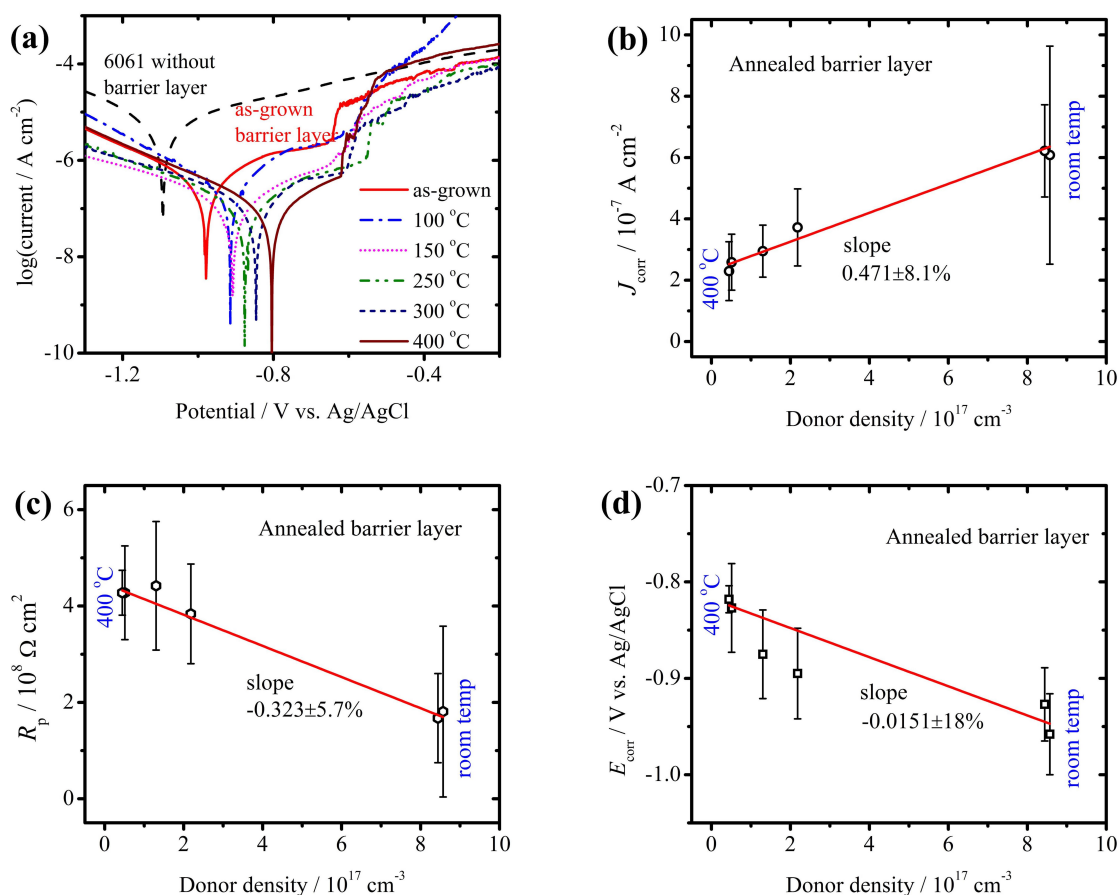


Figure 4. Potentiodynamic polarization curves of the AAO and correlations between corrosion parameters and donor density. (a) Potentiodynamic polarization curves at scan rate $5 \text{ mV}\cdot\text{s}^{-1}$ show the anticorrosion trend. Linear correlation is displayed between (b) corrosion current, (c) polarization resistance of the AAO layer and its donor density. Considerable deviation is shown in the correlation between (d) corrosion potential and donor density.

It is particularly intriguing to attain a linear correlation between corrosion current J_{corr} and donor density N_{d} , as shown in Figure 4b. Such a linear correlation can also be found between polarization resistance R_{p} and N_{d} , Figure 4c. In contrast to J_{corr} and R_{p} , corrosion potential E_{corr} appears less correlated to N_{d} , Figure 4d. The above statement is vindicated in the percent deviation of linearity, which is 18% between E_{corr} and N_{d} , substantially higher than the percent deviation between J_{corr} and N_{d} , 8.1%, also much higher than the percent deviation between R_{p} and N_{d} , 5.7%. The linear correlation is a strong piece of evidence supporting the view that n-type defects are the origin of chloride anion corrosion. We also try to correlate corrosion parameters with acceptor density and obtain a much higher percent deviation of 32% between E_{corr} and N_{a} , 38% between J_{corr} , and N_{a} , 38% between R_{p} and N_{a} (Figure S3, Supplementary Materials). Evidently, the p-type defects are not the reason of corrosion.

It seems worthwhile to discuss the reason why corrosion potential E_{corr} is less correlated to donor density N_{d} in contrast to the superior correlation between J_{corr} and N_{d} , and also that between R_{p} and N_{d} . The reported N_{d} value has been extracted from the linear portion of Mott-Schottky plot, denoting the donor density of the average coating surface. Considering the surface area of our samples, 15.4 cm², certain inhomogeneity is bound to exist on the coating. A good correlation between J_{corr} and N_{d} suggests that the corrosion current is the sum of individual contribution by the typical donor defects, so is R_{p} and N_{d} . However, the corrosion potential is not a sum of individual potentials of point defects. The E_{corr} value is more likely influenced by a small group of point defects that do not contribute to corrosion current.

Etching in sulfuric acid offers a different way to identify which side of the barrier layer is n-type. Mott-Schottky plots of the 400 °C-annealed and etched samples are plotted in Figure 5. We note that the C_{SC}^{-2} values of the etched samples are less than those of unetched samples in Figure 2f, indicating that C_{SC} increases in magnitude. In terms of slope decline, the positive slope decreases more than the negative slope does. Hence, the rise in N_{d} is more pronounced than that in N_{a} after etching. For example, etching for 15 min, the correlated N_{a} value rises from 1.6×10^{16} to 8.6×10^{17} cm⁻³; while the correlated N_{d} value increases more significantly, from 4.5×10^{16} to 1.8×10^{19} cm⁻³ as shown in Figure 5a. Figure 5b presents the Mott-Schottky plot after 45 min etching, the positive slope is almost zero. The above etching results indicate more donor defects after oxide removal. A plausible explanation is that when the vulnerable oxide being etched, more defects and higher surface heterogeneity are created at the same time.

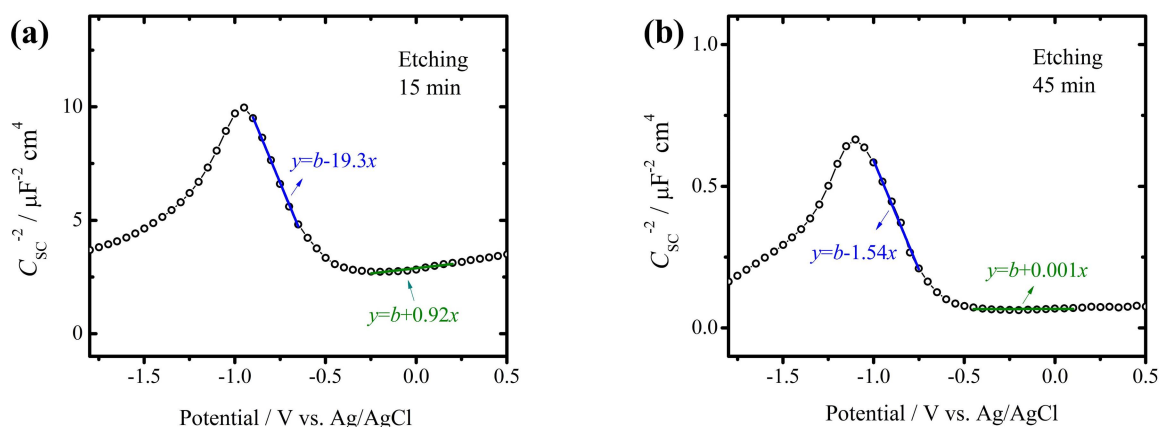


Figure 5. Mott-Schottky plots of the etched AAO layers. The samples of barrier layer have been 400 °C annealed for 1 h are then etched in sulfuric acid for (a) 15 and (b) 45 min. Note the positive slope flattens as etching time increases.

In view of the preferential etching on n-type oxide, the oxide/electrolyte interface ought to be assigned as the donor interface since the preferential etched surface must directly face the sulfuric acid. Furthermore, this assignment is also supported by the correlation results of Figure 4. Only when the oxide/electrolyte (external) interface is n-type, the corrosion protection could be hinged on the donor

density. Otherwise, corrosion of this barrier layer would depend on the acceptor density. Our conclusion on the n-type oxide/electrolyte interface is consistent with the conclusions of Vrublevsky [20–23] and Benfedda [24].

3.2. The PEO Coating with Pre-Grown AAO

The morphological features of the PEO coating are shown in Figure 6. The sample has been pre-anodized under 200 V (+)/40 V (−), then micro-arc treated at 0.7 A (+)/0.8 A (−). The coating thickness is 760 ± 35 nm, Figure 6a, much thicker than its pre-anodized barrier layer, considering the PEO period is 2 min only. Electrical discharges of PEO leave scars, which may be elusive in the cross-sectional image of the coating, yet distinct in the top-view image as shown in Figure 6b. The coating surface shows many pin holes of submicron size associated with a terrain of frozen lava swellings, much different from the pre-anodized surface. Also encircled in red are a few micron-sized grains of hexagonal facet, which might be the precursor of alpha alumina. The crystalline phase of the PEO coating is gamma aluminum oxide, as indicated in its X-ray diffraction result (Figure S4, Supplementary Materials).

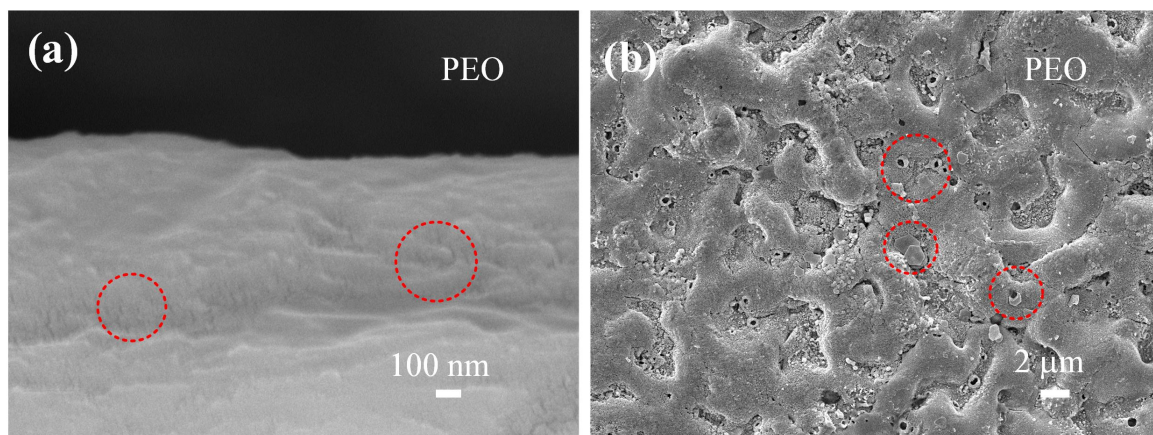


Figure 6. Morphology of the PEO coating with pre-anodized oxide. The SEM images of (a) cross-sectional view and (b) top view of the PEO coating, which is preceded by an AAO layer prepared at 200 V (+)/40 V (−). Large circles mark the electrical discharge damages.

Mott-Schottky plots of two PEO samples are shown in Figure 7, indicating only the n-type behavior is detected. One PEO sample has been treated with a pre-anodized layer without annealing, Figure 7a, the other with a pre-anodized layer being 250 °C-annealed, Figure 7b. Annealing temperature can affect the donor density of the PEO coating. Without annealing, the donor density is $2.92 \times 10^{17} \text{ cm}^{-3}$. The donor density of PEO coating decreases with increasing pre-annealing temperature, with 2.67×10^{17} (150 °C), 2.37×10^{17} (250 °C), and $1.95 \times 10^{17} \text{ cm}^{-3}$ (400 °C).

Since the extent of N_d decline in PEO coating is narrow, its influences on corrosion protection are moderate. Figure 8 shows how much corrosion protection is affected by the donor density of PEO coating. Figure 8a indicates the corrosion potential E_{corr} increases with increasing annealing temperature of the AAO layer, -0.77 ± 0.055 V (without annealing), -0.74 ± 0.03 V (250 °C annealed AAO), -0.72 ± 0.02 V (400 °C annealed AAO). The corrosion current J_{corr} of PEO coating decreases with increasing annealing temperature; $(3.3 \pm 0.9) \times 10^{-8}$ (AAO without annealing), $(1.7 \pm 0.5) \times 10^{-8}$ (250 °C annealed AAO), $(1.7 \pm 0.4) \times 10^{-8} \text{ A}\cdot\text{cm}^{-2}$ (400 °C annealed AAO). And the polarization resistance R_p increases with increasing annealing temperature; $(1.1 \pm 0.3) \times 10^9$ (AAO without annealing), $(2.3 \pm 0.8) \times 10^9$ (250 °C annealed AAO), $(2.1 \pm 0.4) \times 10^9 \Omega \text{ cm}^2$ (400 °C annealed AAO).

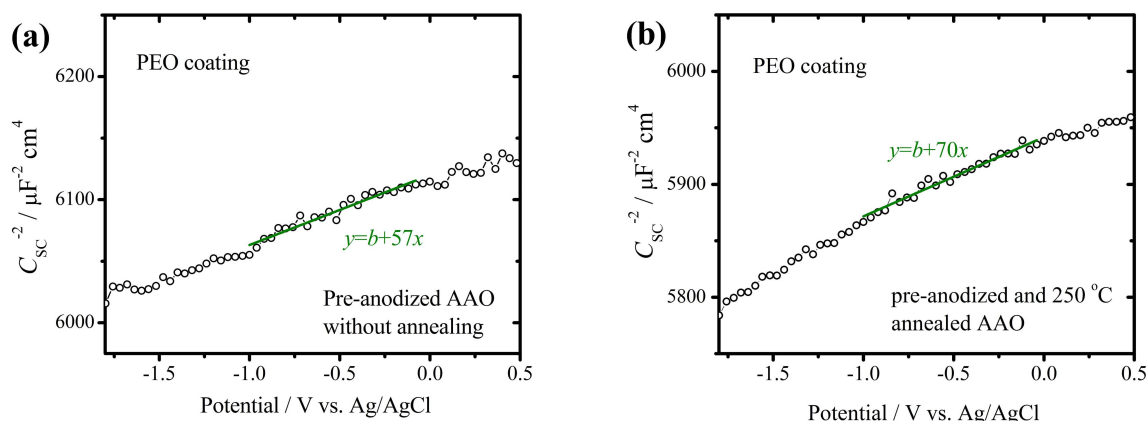


Figure 7. Typical Mott-Schottky plots of the PEO coatings. The plots of C_{SC}^{-2} versus electrode potential are drawn for the PEO coatings with an AAO layer (a) without annealing, (b) 250 °C annealing.

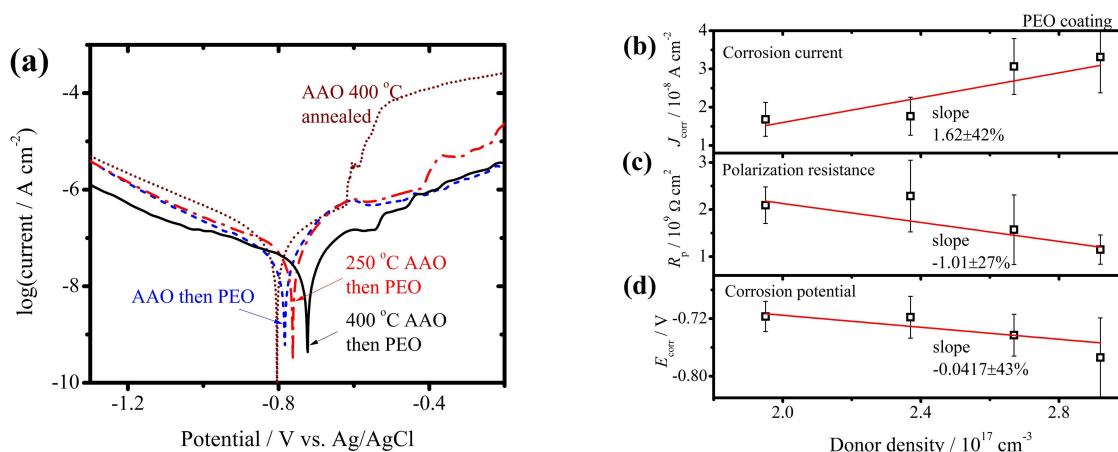


Figure 8. Influences of the AAO layer on anticorrosion of following PEO coating. Comparison of potentiodynamic polarization curves at scan rate $5 \text{ mV}\cdot\text{s}^{-1}$ shows (a) the influences of annealing temperature on anticorrosion of its PEO coating. Correlation between donor density and (b) corrosion current, (c) polarization resistance, (d) corrosion potential of the PEO coating.

We ought to mention that linear correlation of the PEO coating contains substantial uncertainty inferior to that of the AAO layer. Correlation between corrosion protection and donor density of PEO coatings, the percent deviation is 27% between R_p and N_d , 42% between J_{corr} and N_d , 43% between E_{corr} and N_d . We attribute the weak correlation to the damaging effects of electrical discharge. Extra thickness of the PEO coating provides additional protection, but its porosity also brings more uncertainty.

It is of interest to look into why the donor density of PEO coating is affected by annealing temperature of its pre-anodized AAO. One plausible cause is defects of the pre-anodized AAO layer alter the voltage profile of PEO treatment. Figure 9a contrasts the voltage-time profiles of 400 and 250 °C annealed samples, with that of the sample without annealing. The voltage profiles of 400 and 250 °C annealing are consistently higher than that of the one without annealing. Thus, a higher positive voltage is required for the AAO layer of less defects to reach the preset current density. If the pre-anodized layer is partially etched away, the remaining oxide affects the voltage-time profile of PEO differently. Figure 9b compares the voltage profile of the pre-anodized sample without etching with those of the etched samples. As a whole, the positive voltage of the samples etched for 15, 30, 45, and 60 min begins with a lower value than the unetched sample. However, the voltage of etched samples surpasses that of the unetched sample after 5 or 9 s. We generally observe the first spark at 10 s (Video S1, Supplementary Materials), therefore, the E_{10s} value is physically meaningful. The E_{10s} values in Figure 9b are listed as: 507 (15 min), 475 (30 min), 461 (45 min), 437 (60 min), and 421 V

(unetched). An etched sample seems to develop a coating with higher dielectric strength than the unetched sample after several PEO seconds, so that its positive voltage is higher. Therefore, defects of the pre-anodized oxide exert influences on its following PEO coating. Compared with the unetched sample, the etched AAO layer grows faster, so does the positive voltage when PEO time is between 2 and 18 s. The acceptor defects and diminished outer layer seem to be responsible for the fast growth in this brief period.

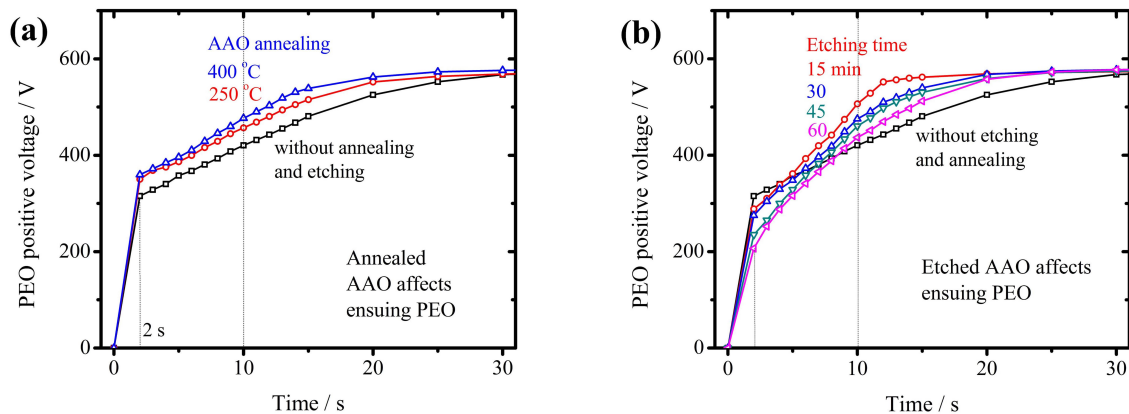


Figure 9. Positive voltage evolution in the initial stage of PEO treatment. Comparison of the voltage-time profiles of PEO that began with (a) 400 and 250 °C annealed barrier layer, and the barrier layer without annealing. Comparison of the voltage-time profiles of PEO that started with (b) the barrier layers of 15, 30, 45, and 60 min etching and the barrier layer without etching and annealing.

4. Conclusions

Point defects are known to affect corrosion protection properties in various manners, but researchers seldom connect the two directly. In this research, the point defect densities of acceptor and donor are varied through annealing and etching of the AAO layer, and the anticorrosion parameters of the AAO layer are measured with potentiodynamic polarization scans. We find that a linear correlation between corrosion current and donor density, also between polarization resistance and donor density. The correlation between corrosion potential and donor density can be fitted with considerable deviation. For PEO coatings, only the n-type behavior is observed. Similar correlations can be established between the corrosion properties and donor density for PEO coating. However, deviations from linear correlation are substantial, since the electrical discharges during PEO introduce porosity and uncertainty in anticorrosion properties.

Supplementary Materials: The following are available online at <http://www.mdpi.com/2079-6412/10/1/20/s1>, Figure S1: Schematic diagram of setup for anodizing the 6061 sample, following by PEO treatment, Figure S2: Experimental procedure of electrochemical oxidation, characterization, and corrosion analysis, Figure S3: Linear correlation between corrosion parameters and acceptor density. In contrast to Figure 4b–d, the correlations are poor with respect to acceptor density. Correlation is attempted between (a) J_{corr} and N_a , (b) R_p and N_a , (c) E_{corr} and N_a , Figure S4: XRD patterns of AAO and PEO coatings. (a) The result of 400 °C annealed barrier layer displays the diffraction lines of metallic aluminum substrate only. (b) The diffraction result of PEO coating that began with an AAO precursor shows the gamma aluminum oxide features in addition to the diffraction lines of aluminum metal, Video S1: The first appearance of microdischarges in PEO.

Author Contributions: Conceptualization, formal analysis and writing, D.-S.T.; investigation and validation, H.-R.L.; resources, C.-C.C. All authors have read and agreed to the published version of the manuscript.

Funding: The authors would like to thank Ministry of Science and Technology of Taiwan for financial support of this work through the project MOST-106-2221-E-011-119-MY3.

Acknowledgments: We would like to thank Ching-Hwa Ho of NTUST for allowing the oscilloscope and other electronic measurement instruments in this work.

Conflicts of Interest: The authors declare no conflict of interest.

References

1. Clyne, T.W.; Troughton, S.C. A review of recent work on discharge characteristics during plasma electrolytic oxidation of various metals. *Int. Mater. Rev.* **2018**, *63*, 127–164. [[CrossRef](#)]
2. Liu, C.Y.; Tsai, D.S.; Wang, J.M.; Tsai, J.T.J.; Chou, C.C. Particle size influences on the coating microstructure through green chromia inclusion in plasma electrolytic oxidation. *ACS Appl. Mater. Interfaces* **2017**, *9*, 21864–21871. [[CrossRef](#)] [[PubMed](#)]
3. Tsai, D.S.; Chen, G.W.; Chou, C.C. Probe the micro arc softening phenomenon with pulse transient analysis in plasma electrolytic oxidation. *Surf. Coat. Technol.* **2019**, *357*, 235–243. [[CrossRef](#)]
4. Matykina, E.; Arrabal, R.; Skeldon, P.; Thompson, G.E.; Belenguer, P. AC PEO of aluminum with porous alumina precursor films. *Surf. Coat. Technol.* **2010**, *205*, 1668–1678. [[CrossRef](#)]
5. Matykina, E.; Arrabal, R.; Mohamedm, A.; Skeldon, P.; Thompson, G.E. Plasma electrolytic oxidation of pre-anodized aluminum. *Corros. Sci.* **2009**, *51*, 2897–2905. [[CrossRef](#)]
6. Lee, W.; Park, S.J. Porous anodic aluminum oxide: Anodization and templated synthesis of functional nanostructures. *Chem. Rev.* **2014**, *114*, 7487–7556. [[CrossRef](#)]
7. Thompson, G.E. Porous anodic alumina: Fabrication, characterization and applications. *Thin Solid Films* **1997**, *297*, 192–201. [[CrossRef](#)]
8. Hourdakakis, E.; Koutsourelis, M.; Papaioannou, G.; Nassiopoulou, A.G. Leakage current and charging discharging processes in barrier-type anodic alumina thin films for use in metal-insulator-metal capacitors. *J. Appl. Phys.* **2018**, *123*, 215301. [[CrossRef](#)]
9. Mibus, M.; Jensen, C.; Hu, X.; Knospe, C.; Reed, M.L.; Zangari, G. Dielectric breakdown and failure of anodic aluminum oxide films for electrowetting systems. *J. Appl. Phys.* **2013**, *114*, 014901. [[CrossRef](#)]
10. Capraz, O.O.; Overmeere, Q.V.; Shrotriya, P.; Herbert, K.R. Stress induced by electrolyte anion incorporation in porous anodic aluminum oxide. *Electrochim. Acta* **2017**, *238*, 368–374. [[CrossRef](#)]
11. Capraz, O.O.; Shrotriya, P.; Skelton, P.; Thompson, G.E.; Herbert, K.R. Factors controlling stress generation during the initial growth of porous anodic aluminum oxide. *Electrochim. Acta* **2015**, *159*, 16–22. [[CrossRef](#)]
12. Dou, Q.; Overmeere, Q.V.; Shrotriya, P.; Li, W.; Herbert, K.R. Stress induced by incorporation of sulfate ions into aluminum oxide films. *Electrochem. Commun.* **2018**, *88*, 39–42. [[CrossRef](#)]
13. Stojadinovic, S.; Vasilic, R.; Nedic, Z.; Kasalica, B.; Belca, I.; Zekovic, L. Photoluminescent properties of barrier aluminum oxide films on aluminum. *Thin Solid Films* **2011**, *519*, 3516–3521. [[CrossRef](#)]
14. Nigo, S.; Kubota, M.; Harada, Y.; Hirayama, T.; Kato, S.; Kitazawa, H.; Kido, G. Conduction band caused by oxygen vacancies in aluminum oxide for resistance random access memory. *J. Appl. Phys.* **2012**, *112*, 033711. [[CrossRef](#)]
15. Chang, J.K.; Liao, C.M.; Chen, C.H.; Tsai, W.T. Microstructure and electrochemical characteristics of aluminum anodized film formed in ammonium adipate solution. *J. Electrochem. Soc.* **2003**, *150*, B266–B273. [[CrossRef](#)]
16. Sousa, C.T.; Leitao, D.C.; Proenca, M.P.; Apolinario, A.; Correia, J.G.; Ventura, J.; Araujo, J.P. Tuning pore filling of anodic alumina templates by accurate control of the bottom barrier layer thickness. *Nanotechnology* **2011**, *22*, 315602. [[CrossRef](#)]
17. Diggle, J.W.; Downie, T.C.; Goulding, C.W. Anodic oxide films on aluminum. *Chem. Rev.* **1969**, *69*, 365–405. [[CrossRef](#)]
18. Takahashi, H.; Kasahara, K.; Fujiwara, K.; Seo, M. The cathodic polarization of aluminum covered with anodic oxide films in a neutral borate solution. *Corros. Sci.* **1994**, *36*, 677–688. [[CrossRef](#)]
19. Mibus, M.; Jensen, C.; Hu, X.; Knospe, C.; Reed, M.L.; Zangari, G. Improving dielectric performance in anodic aluminum oxide via detection and passivation of defect states. *Appl. Phys. Lett.* **2014**, *104*, 244103. [[CrossRef](#)]
20. Vrublevsky, I.; Jagminas, A.; Schreckenbach, J.; Goedel, W.A. Electronic properties of electrolyte/anodic alumina junction during porous anodizing. *Appl. Surf. Sci.* **2007**, *253*, 4680–4687. [[CrossRef](#)]
21. Vrublevsky, I.; Jagminas, A.; Schreckenbach, J.; Goedel, W.A. Embedded space charge in porous alumina films formed in phosphoric acid. *Electrochim. Acta* **2007**, *53*, 300–304. [[CrossRef](#)]
22. Vrublevsky, I.; Parkoun, V.; Schreckenbach, J.; Goedel, W.A. Dissolution behavior of the barrier layer of porous oxide films on aluminum formed in phosphoric acid studied by a re-anodizing technique. *Appl. Surf. Sci.* **2006**, *252*, 5100–5108. [[CrossRef](#)]

23. Vrublevsky, I.; Parkoun, V.; Sokol, V.; Schreckenbach, J. Study of chemical dissolution of the barrier oxide layer of porous alumina films formed in oxalic acid using a re-anodizing technique. *Appl. Surf. Sci.* **2004**, *236*, 270–277. [[CrossRef](#)]
24. Benfedda, B.; Hamadou, L.; Benbrahim, N.; Kadri, A.; Chainet, E.; Charlot, F. Electrochemical impedance investigation of anodic alumina barrier layer. *J. Electrochem. Soc.* **2012**, *159*, C372–C381. [[CrossRef](#)]
25. Hassel, A.W.; Lohrengel, M.M. Initial stages of cathodic breakdown of thin anodic aluminum oxide films. *Electrochim. Acta* **1995**, *40*, 433–437. [[CrossRef](#)]
26. Hassel, A.W.; Diesing, D. Modification of trap distributions in anodic aluminum tunnel barriers. *J. Electrochem. Soc.* **2007**, *154*, C558–C561. [[CrossRef](#)]
27. Schultze, J.W.; Lohrengel, M.M. Stability, reactivity and breakdown of passive films. *Electrochim. Acta* **2000**, *45*, 2499–2513. [[CrossRef](#)]
28. Yeh, S.C.; Tsai, D.S.; Wang, J.M.; Chou, C.C. Coloration of aluminum alloy surface with dye emulsions while growing a plasma electrolytic oxide layer. *Surf. Coat. Technol.* **2016**, *287*, 61–66. [[CrossRef](#)]
29. Hunter, M.S.; Fowle, J. Determination of barrier layer thickness of anodic oxide coatings. *J. Electrochem. Soc.* **1954**, *101*, 481–485. [[CrossRef](#)]



© 2019 by the authors. Licensee MDPI, Basel, Switzerland. This article is an open access article distributed under the terms and conditions of the Creative Commons Attribution (CC BY) license (<http://creativecommons.org/licenses/by/4.0/>).